01,14

Anomalous mechanical behavior of ultrafine-grained Al−Mg−Zr alloy at low temperature

© D.I. Sadykov[1,2], M.Yu. Murashkin[3], D.A. Kirilenko[1], A.A. Levin[1], A.I. Lihachev[1], T.S. Orlova[1,¶]

[1] Ioffe Institute,
St. Petersburg, Russia
[2] Institute of Advanced Data Transfer Systems, ITMO University,
St. Petersburg, Russia
[3] Ufa University of Science and Technology,
Ufa, Russia

¶ E-mail: orlova.t@mail.ioffe.ru

Received May 13, 2024
Revised May 13, 2024
Accepted May 14, 2024

The effect of deformation temperature on strength and ductility of ultrafine-grained (UFG) low-alloyed Al−Mg−Zr alloy before and after special deformation-heat treatment (DHT) consisting of low-temperature short-term annealing and a small additional deformation, was investigated in the temperature range 77−293 K. UFG structure was obtained by high-pressure torsion processing. It has been established that DHT leads to a substantially enhanced ductility (7−13%) while maintaining high strength (yield stress ∼ 300−435 MPa, ultimate tensile strength ∼ 370−490 MPa) over the entire temperature range studied. In the post-DHT state, an anomalous character of temperature dependences of the strength and ductility in the temperature range of 243−293 K is observed for the first time, which is unusual for coarse-grained and UFG Al-based alloys. A possible explanation for such anomalous temperature dependences of strength and ductility is proposed, based on the competition between various thermally activated processes at grain boundaries with inverse temperature dependences.

Keywords: Aluminum alloys, ultrafine-grained microstructure, ductility, strength, grain boundaries.

DOI: 10.61011/PSS.2024.06.58633.119

1. Introduction

Al−Mg-based alloys are a promising alternative to expensive stainless steel, nickel steel, and invar alloys as cryogenic materials for the needs of the aerospace industry, arctic shipbuilding, and also for hydrogen storage applications [1–3] due to their lightweight, good workability, and weldability.

The key disadvantage of Al−Mg alloys compared to the above materials is their relative low strength. One of the effective and promising ways to significantly increase the strength of Al−Mg-based alloys is grain refinement up to formation of an ultrafine-grained (UFG) or nanocrystalline (NC) structure through severe plastic deformation (SPD) treatment [4]. Nowadays, there are many SPD methods [4], among them the most widespread ones are high-pressure torsion (HPT) [5], equal channel angular pressing (ECAP) [6], accumulative roll bonding (ARB) [7], constrained groove pressing (CGP) [8], and multi-axial forging (MAF) [9]. In addition to the classical SPD methods, combinations of SPD methods and additive manufacturing techniques are used in some cases [10]. As was shown in [5,8,11], UFG and NC bulk Al−Mg materials indeed demonstrate excellent strength properties but, unfortunately, low ductility ($\leq 3\%$), which does not meet the requirement of industrial applications [12,13]. Thus, the problem of increasing ductility while maintaining high strength of UFG and NC bulk materials is very important.

Recently, a new effective approach has been proposed to achieve high strength and high ductility at room temperature (RT) in UFG commercially pure (CP) Al and some UFG Al-based alloys subjected to HPT [14,15]. The approach is based on a special deformation-heat treatment (DHT) of the material after initial structuring by HPT. The DHT consists of short-term low temperature annealing and subsequent small additional HPT deformation at RT [14,15]. The phenomenon of increase in ductility due to deformation after appropriate annealing is unusual for coarse-grained (CG) materials and is called the deformation-induced softening (DIS) effect [15,16].

The significant improvement of ductility of HPT-processed Al by such DHT is related to introduction of additional dislocation density into the structure of grain boundaries (GBs) relaxed after annealing while maintaining an almost unchanged grain size [15,17].

These investigations have shown that changing the structure (state) of GBs can substantially modify both strength and ductility of Al and its alloys with UFG structures. Recently, this approach has also been successfully applied to UFG Al-0.53Mg-0.27Zr (wt.%) alloy structured by HPT [18]. As a result of a similar DHT, a significant increase in ductility (δ) from $< 2\%$ to $\sim 9\%$ was achieved while maintaining high strength (ultimate tensile strength $\sigma_{UTS} \sim 390$ MPa) for the UFG Al-0.53Mg-0.27Zr (wt.%) alloy. In the case of the UFG Al-0.53Mg-0.27Zr (wt.%) alloy,

the DIS effect has been explained by the introduction of an additional density of extrinsic grain boundary dislocations (EGBDs) at GBs by a small additional deformation. Such induced EGBDs increase the degree of nonequilibrium of the GBs, they are not pinned by the segregated Mg atoms [18] and can form grain boundary dislocation pile-ups at triple junctions under external loading and, hence, contribute to the emission of a larger number of lattice dislocations from the GBs under a relatively lower stress [15,18].

For the potential use of UFG Al-Mg based alloys at low temperatures (including cryogenic ones), it is necessary to understand how the achieved combination of properties (strength and ductility) will behave when the temperature decreases. The mechanical behavior of Al-Mg based alloys at low temperatures has been poorly studied to date. To the best of our knowledge, only a few studies have been carried out for UFG and CG Al-Mg based alloys [2,19–23]. The effect of grain refinement (UFG structure) on mechanical properties was mainly studied at room and cryogenic temperatures (77–110 K). In Ref. [2,19–23], there are no data on the mechanical behavior of UFG and CG Al-Mg alloys in the temperature range 223–293 K, which is extremely important for the aviation industry, infrastructure and marine operating in severe northern (arctic) conditions.

It is important to note that any studies on the influence of the GB state in UFG Al-Mg alloys on the mechanical behavior at low temperature have not been reported. However, as was shown in [24–27], the change in the GB state [24–26] or GB character [27] without any significant changing the grain size can remarkably affect the mechanical properties of UFG Al and some UFG Al-based alloys, both at room temperature and low temperatures.

The aim of the present work is to study the mechanical behavior of UFG low-doped Al-Mg-Zr alloy in a temperature range of 77–293 K. The article is focused on the effect of GB state on the behavior of strength and ductility of the UFG alloy with decreasing temperature. A special attention is paid to the temperature range 223–293 K, which is of a special interest for potential applications. Such studies are important not only for potential application of Al-Mg-Zr alloys at decreased temperatures and also for better understanding physical reasons of the DIS effect in this system. The role of grain boundary state in realization of good ductility and abnormal change of strength and ductility with decreasing temperature will be established.

2. Materials and methods

The Al-0.95Mg-0.32Zr (wt.%) alloy obtained by casting and subsequent hot rolling [28] was chosen for the study. The more detailed chemical composition (98.58Al, 0.95Mg, 0.32Zr, 0.03Fe, 0.056Si, 0.012(Ti+V+Cr+Mn), others 0.052 (wt.%)) of the alloy was determined with a Bruker Q4 Tasman optical emission spectrometer.

To homogenize the solid solution and to achieve the formation of a nanosized precipitates of the Al_3Zr phase ($L1_2$), the alloy was subjected to artificial aging at 375°C for 140 h [29].

The initial UFG structure was obtained by HPT at RT (293 K) under an applied pressure of 2 GPa with the number of turns $n = 10$ (HPT state). A part of the HPT processed samples in the form of disks with a diameter of 20 mm and a thickness of 1.5 mm was subjected to additional annealing at 150°C for 1 h (HPT+AN state) and subsequent additional HPT deformation to $n = 0.25$ turns (HPT+AN+0.25HPT state). Thus, the initial HPT-processing and additional DHT were performed in the same conditions as in the case of Al-0.53Mg-0.27Zr (wt.%) alloy [18].

X-ray diffraction (XRD) measurements were carried out in the $\theta-2\theta$ scan mode using the D2 Phaser X-ray diffractometer (Bruker AXS, Karlsruhe, Germany), constructed in vertical Bragg–Brentano geometry and equipped with a linear semiconductor position-sensitive detector LYNXEYE (Bruker AXS) and an X-ray tube with a copper anode and a Ni-foil K_β-filter (Cu-K_α radiation with a mean wavelength $\lambda = 1.5418$ Å). In order to correct the XRD patterns for zero shift and displacement, additional measurements were performed of samples placed in NaCl powder (calibrated using the Si640f XRD powder standard (NIST, Gaithersburg, Maryland, USA)), so that the surface of the sample was flush with the surface of the NaCl powder.

The measured XRD reflections were treated using *EVA* software (Diffrac. Suite EVA Version 5.1.0.5, Bruker AXS GmbH, Karlsruhe, Germany, 2019) in combination with the Powder Diffraction File-2 database (PDF-2, release 2014, International Centre for Diffraction Data (ICDD). Newton Square, PA, USA). Main structural and microstructural parameters, such as the cubic unit cell parameter (a), the average size of the coherently scattering domains (D_{CSD}), the average absolute value of microstrain ε_s (known also as level of elastic microdistortion $\langle\varepsilon^2\rangle^{1/2}$) were calculated using *Celsiz* and *SizeCr* software (see Ref. [17] for brief descriptions of the programs). The dislocation density (L_{dis}) was estimated using equation [30]:

$$L_{dis} = \frac{2\sqrt{3}\langle\varepsilon^2\rangle^{1/2}}{D_{CSD} \cdot b}, \quad (1)$$

where b is the value of Burgers vector of lattice dislocation ($b = 0.286$ nm for Al [31]).

Microstructures were characterized by (scanning) transmission electron microscopy (TEM/STEM) using microscope JEOL JEM-2100 F (JEOL Ltd., Tokyo, Japan) with accelerating voltage 200 kV, point resolution 0.19 nm. The microscope is equipped with the unit for conducting *in-situ* energy dispersive X-ray analysis (EDX analysis). Electron backscatter diffraction (EBSD) measurements were carried out using scanning electron microscope (SEM) JSM 7001 F (JEOL Ltd., Tokyo, Japan) equipped with HKL Nordlys EBSD detector (Oxford Instruments, Abingdon-on-Thames, UK) and Channel 5 software. The size of the scanning area was $20 \times 20\,\mu m^2$, the scanning step was 50 nm.

The resulting EBSD maps included at least 1000 grains for each state and were used to determine the average grain size (d_{av}^{G}), the proportion of high-angle grain boundaries ($f_{\geq 15}$), and the average misorientation angle (θ_{av}). Further experimental details of EBSD, XRD, and TEM measurements and data analysis are presented in [17].

For mechanical tensile tests the samples with a gauge size of $2.0 \times 6.0 \times 1.0\,mm^3$ were cut from the HPT-processed disks with and without additional DHT at a distance of 5 mm from disk center. The tensile tests were carried out on Shimadzu AG-50kNX machine (Shimadzu Corp., Kyoto, Japan) at a constant strain rate of $5 \cdot 10^{-4}\,s^{-1}$. The effect of deformation temperature (T_{def}) on mechanical properties was studied in the temperature range from 293 to 77 K (in liquid nitrogen) using thermostatic chamber TCE-N300 (Shimadzu Corp., Kyoto, Japan) cooled by nitrogen gas or liquid nitrogen. T_{def} was stabilized with an accuracy of ± 0.5 K. The main mechanical characteristics, such as yield stress ($\sigma_{0.2}$), ultimate tensile strength (σ_{UTS}), elongation to failure (δ), and uniform elongation (δ_1) were determined from the tensile stress-strain diagrams.

Some control measurements of the electrical conductivity (ω) of samples in the UFG state were carried out before and after applying DHT using an eddy current electrical conductivity meter (VE-27NTS, OOO NPP „SIGMA“, Ekaterinburg, Russia) with an accuracy of $\pm 2\%$. The measurements were carried out at room temperature at a distance of 5 mm from the centers of the HPT disks, in the same location where the microstructure was characterized.

3. Experimental results

3.1. Mechanical properties

Figure 1 shows stress-strain diagrams obtained at RT and decreased deformation temperatures ($T_{def} = 263$, 243 and 193 K are taken as an example) for the UFG alloy Al-0.95Mg-0.32Zr (wt.%) in all three studied states. The corresponding mechanical characteristics ($\sigma_{0.2}$, σ_{UTS}, δ, δ_1) are listed in Table 1.

As is seen from analysis of stress-strain diagrams at RT (Figure 1, *a*, Table 1), annealing at 150°C for 1 h led to a decrease in strength and ductility compared to the initial HPT state. The value of $\sigma_{0.2}$ decreased from ~ 420 to ~ 370 MPa. The ductility (elongation to failure δ) decreased from 1.6 to 0.6%. Additional deformation by 0.25 turns (HPT+AN+0.25HPT state) led to a significant increase in ductility from $\delta < 1\%$ after annealing (Table 1) to $\delta \sim 7\%$ after additional HPT while maintaining a high level of strength ($\sigma_{0.2} \sim 370$ MPa, $\sigma_{UTS} \sim 460$ MPa). Thus, the DIS effect also exists in the UFG Al-0.95Mg-0.32Zr (wt.%) alloy structured by HPT. Almost twice the higher concentration of Mg in the Al-0.95Mg-0.32Zr (wt.%) alloy compared to the Al-0.53Mg-0.27Zr (wt.%) alloy [18] leads to slightly lower ductility achieved after applying the same DHT, but to higher strength.

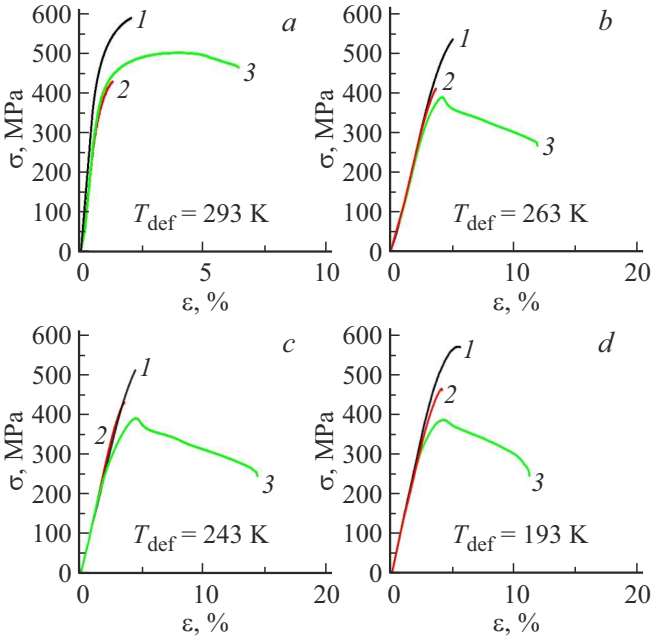

Figure 1. Stress–strain diagrams of Al-0.95Mg-0.32Zr (wt.%) alloy in the HPT (*1*), HPT+AN (*2*), HPT+AN+0.25HPT (*3*) states at various temperature: *a*) 293 K, *b*) 263 K, *c*) 243 K, *d*) 193 K.

The temperature dependences of the $\sigma_{0.2}$ and δ for all studied states are shown in Figure 2. In the HPT state, the value of $\sigma_{0.2}$ gradually increases from ~ 420 to ~ 560 MPa in the entire studied range of T_{def} (Figure 2, *a*, Table 1). The value of δ remains very low in the whole temperature range 77–293 K: it slowly decreases from 1.6 to $\sim 0.4\%$ with decreasing T_{def} from 293 to 253 K (Figure 2, *c*, Table 1). With a further decrease in T_{def}, the value of δ increases only slightly up to 1.4% at 77 K. Such low ductility in the range of cryogenic temperatures (77–110 K) is not typical for a number of UFG Al-based alloys such as Al-Cu-Zr [26], Al-Mg-Mn-Sc-Zr [19,20] and coarse-grained Al-Mg-Si-Fe-Cr [21], AA6061 [22,23], AA5052, and AA5086 [2] aluminum alloys.

In the HPT+AN state, the value of $\sigma_{0.2}$ increases monotonously from ~ 370 to ~ 410 MPa with a decrease of T_{def} from 293 to 193 K (Figure 2, *a*, Table 1). The value of δ practically does not change and remains extremely low (0.5–0.6%) in the T_{def} range of 193–293 K (Figure 2, *c*, Table 1).

The character of the $\sigma_{0.2}(T_{def})$ dependence for the alloy in the HPT+AN+0.25HPT state is different compared to the cases of the HPT and HPT+AN states. With a decrease in T_{def} from 293 to 243 K, $\sigma_{0.2}$ decreases from ~ 370 to ~ 300 MPa (Figure 1, *b, c* and Figure 2, *a*, Table 1). With a further decrease in T_{def} to 77 K, a gradual increase in the yield stress up to 435 MPa is observed. The character of temperature dependence of ultimate tensile strength in the HPT+AN+0.25HPT state is approximately the same as the $\sigma_{0.2}(T_{def})$ dependence character (Figure 2, *b*). It should

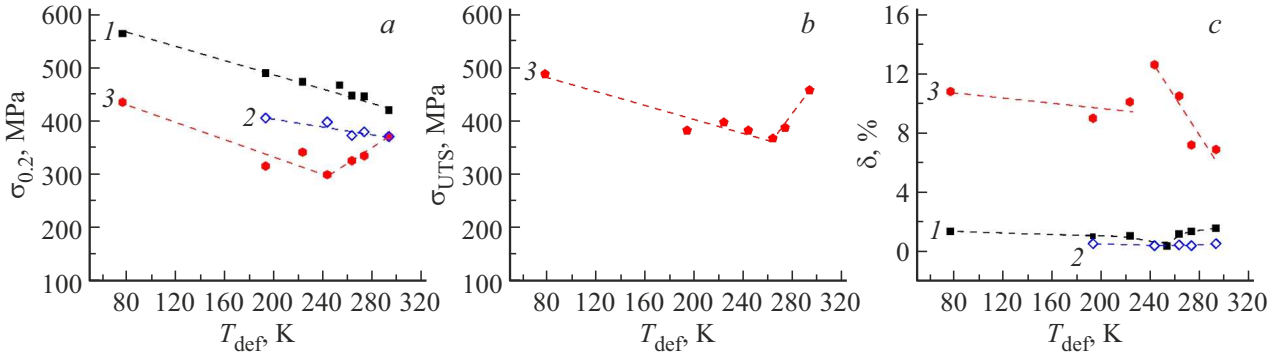

Figure 2. Temperature dependence of the yield stress (*a*), ultimate tensile strength (*b*) and ductility (*c*) of UFG Al-0.95Mg-0.32Zr (wt.%) alloy in various states: *1* — HPT; *2* — HPT+AN; *3* — HPT+AN+0.25HPT. Dashed lines are guide for the eye.

Table 1. Mechanical characteristics of the UFG Al-0.95Mg-0.32Zr (wt.%) alloy in various states at different T_{def}

State	T_{def}, K	$\sigma_{0.2}$, MPa	σ_{UTS}, MPa	δ, %	δ_1, %
HPT	293	420±30	543 ± 20*	1.6 ± 0.5	–
	273	446±5	548 ± 5*	1.4 ± 0.3	–
	263	447±6	543 ± 15*	1.2 ± 0.5	–
	243	467±5	498 ± 15*	0.4 ± 0.1	–
	223	473±5	566 ± 5*	1.1 ± 0.3	–
	193	489±5	563 ± 5*	1.1 ± 0.6	–
	77	563±20	630 ± 20	1.4 ± 0.3	0.9±0.1
HPT+AN	293	371±8	414 ± 5*	0.6 ± 0.1	–
	273	380±5	406 ± 15*	0.4 ± 0.2	–
	263	373±10	400 ± 10*	0.5 ± 0.1	–
	243	398±5	419 ± 10*	0.4 ± 0.1	–
	193	410±25	440 ± 30*	0.6 ± 0.1	–
HPT+AN +0.25HPT	293	371±15	458 ± 18	6.9 ± 1.3	2.6±0.5
	273	336±25	388 ± 20	7.2 ± 4.2	0.9±0.3
	263	317±25	371 ± 20	10.5 ± 1.3	1.2±0.4
	243	300±15	386 ± 20	12.6 ± 1.2	1.7±0.4
	223	342±15	401 ± 15	10.1 ± 0.4	1.3±0.3
	193	316±5	386 ± 5	9 ± 0.5	1.4±0.1
	77	435±20	492 ± 10	10.8 ± 0.6	1.5±0.1

* — this stress value corresponds to the failure stress (σ_f).

be noted that in the HPT and HPT+AN states in the studied deformation temperature range, the samples were fractured almost brittlely (Figure 1, *b, c*, Table 1), without reaching the σ_{UTS} value. Ductility in the temperature range from 293 to 243 K increases from ~ 7 to ~ 13% (Figure 1, *b, c* and Figure 2, *c*, Table 1). With a further decrease in T_{def} to 77 K, the value of δ first decreases to ~ 10% and then δ remains almost unchanged. Thus, the alloy in the HPT+AN+0.25HPT state demonstrates a good level of ductility ($\delta \sim 7-13\%$) and high strength ($\sigma_{0.2} \sim 300-435$ MPa, $\sigma_{UTS} \sim 370-490$ MPa) over the entire deformation temperature range of 77–293 K. It should be noted that the achieved values of ductility in the temperature range of 77–293 K significantly exceed the critical value required for industrial applications [12]. A substantial increase in ductility at $T_{def} = 293$ K due to a similar DHT was obtained earlier for low alloyed Al-Cu-Zr system [26]. However, in the case of Al-Cu-Zr alloy, a decrease in T_{def} led to a decrease in the achieved ductility and the disappearance of the DIS effect around $T_{def} \approx 223$ K [26]. In contrast to the UFG Al-0.95Mg-0.32Zr (wt.%) in the present study, the UFG Al-1.47Cu-0.34Zr (wt.%) alloy [26] demonstrated almost brittle behavior ($\delta < 2\%$) at $T_{def} = 223-243$ K. The UFG CP Al and UFG Al-0.4Zr (wt.%) alloy also do not demonstrate anomalous temperature behavior of mechanical properties after similar DHT [24,25]. All this indicates that it is the presence of Mg that is responsible for the anomalous change in strength and ductility with decreasing temperature in the range 243–293 K.

3.2. Microstructural characterization

It was previously shown that after long-term aging (AG) of low-alloyed Al-0.4Zr (wt.%) [32] and Al-0.53Mg-0.27Zr (wt.%) [28] alloys, numerous nanoprecipitates of the secondary phase Al_3Zr (Ll_2) are formed. However, after structuring by HPT, most of these nanoprecipitates dissolve in the Al lattice. As a result, as was shown in Ref. [32,33], the change in mechanical properties of the HPT-processed Al-0.4Zr (wt.%) alloy with and without preliminary aging are almost the same when DHT is applied. In this work, pre-aging was used only for the purpose of comparing the effect of DHT on the mechanical behavior of the studied Al-Mg-Zr system with other alloys (Al-Zr [32], Al-Cu-Zr [26]), which were subjected to similar pre-aging.

The microstructure of the Al-0.95Mg-0.32Zr (wt.%) alloy in AG state is presented in Figure 3. The microstruc-

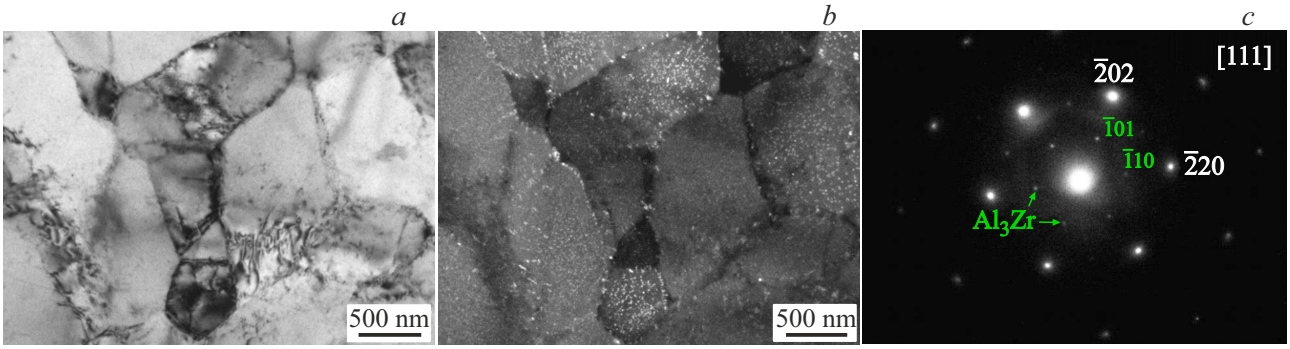

Figure 3. TEM images of Al-0.95Mg-0.32Zr (wt.%) alloy after long-term aging in (*a*) bright field, (*b*) dark field image modes with (*c*) SAED pattern taking along $[111]_{Al}$ zone axis.

Table 2. Microstructure parameters of UFG Al-0.95Mg-0.32Zr (wt.%) in various states

State	EBSD			XRD			
	d_{av}^{G}, nm	$f_{\leq 15}$, %	θ_{av}, °	a, Å	D_{CSD}, nm	ε_s, %	L_{dis}, 10^{13} m^{-2}
HPT	410 ± 60	70.6	28.8 ± 0.3	4.0530 ± 0.0004	119 ± 9	0.064 ± 0.003	6.5 ± 0.6
HPT+AN	470 ± 80	82.2	33.5 ± 0.3	4.0544 ± 0.0002	181 ± 4	0.018 ± 0.001	1.2 ± 0.1
HPT+AN+0.25HPT	480 ± 80	68.9	28.8 ± 0.3	4.0536 ± 0.0002	124 ± 11	0.066 ± 0.004	6.4 ± 1.2

ture of Al-0.95Mg-0.32Zr (wt.%) alloy in the AG state (before HPT processing) is similar to the microstructure which was earlier observed in Al-0.4Zr (wt.%) [32] and Al-0.53Mg-0.27Zr (wt.%) [28] alloys after aging with similar conditions. As a result of aging, nano-sized precipitates with a size of 10−20 nm were formed in aluminum matrix. These precipitates belong to the Al_3Zr (Ll_2) phase that was confirmed by selected area electron diffraction (SAED) in TEM (Figure 3, *c*). The formation of similar precipitates in different aluminum alloys containing Zr was reported by other authors for similar aging conditions [29,34,35].

More detailed characterization of the microstructure of low-alloyed Al-Mg-Zr alloy in the AG state is presented in [28]. In the present work, the main attention was paid to a comparative study of the microstructure in the HPT, HPT+AN, HPT+AN+0.25HPT states in order to identify the key microstructural parameters responsible for the drastic increase in ductility of the UFG Al-Mg-Zr alloy in the temperature rage 77−293 K after application of DHT.

Figure 4 displays typical EBSD maps, and corresponding grain size distributions and distributions of GBs on misorientation angles for these three investigated states. The main structural and microstructural parameters determined using EBSD data are shown in Table 2. All the studied states have an UFG structure with an average grain size (d_{av}^{G}) in the range from ∼ 410 to ∼ 480 nm (Table 2). Moreover, in all the studied states, a predominantly equiaxed grain shape and predominant high-angle misorientations of the GBs (the proportion of GBs with misorientaion angles $\theta \geq 15°$, $f_{\geq 15} > 60\%$) are observed. The grain size distribution is unimodal and practically does not change from state to state (Figure 4, *b, e, h*).

Figure 5 displays typical TEM images of the alloy in three studied states. In the HPT state (Figure 5, *a*), dislocations in grain interiors are practically not observed, with the exception of rare individual dislocations observed in some coarser grains.

Annealing (HPT+AN state) leads to a decrease in the number of dislocations (Figure 5, *b*, Table 2), which is due to the recovery processes. After additional deformation (HPT+AN+0.25HPT state), single dislocations or their arrays near GBs are visible in some grains (Figure 5, *c*). Moreover, in HPT and HPT+AN+0.25HPT states the GBs are curved and fuzzy (Figure 5, *a, c*), which indirectly indicates the nonequilibrium character of the GBs [36]. In the HPT+AN state, the GBs are more clearly defined and straightened, which indicates a greater degree of equilibrium compared to the HPT and HPT+AN+0.25HPT states. The nanosized precipitates observed in the TEM images (Figure 5) are Al_3Zr phase precipitates, which was earlier confirmed by high resolution in STEM [28]. After HPT, only small amount of such precipitates is observed (Figure 5, *a*, indicated by red arrows). They are located non-uniformly, and subsequent DHT practically does not affect their size and number.

Additionally, we measured electrical conductivity in the pre- and post-DHT states. The obtained values are almost identical and equal to 47.5 ± 0.4 and 47.9 ± 0.5% IACS (International Annealed Copper Standard), respectively. Since electrical conductivity is most sensitive to alloying

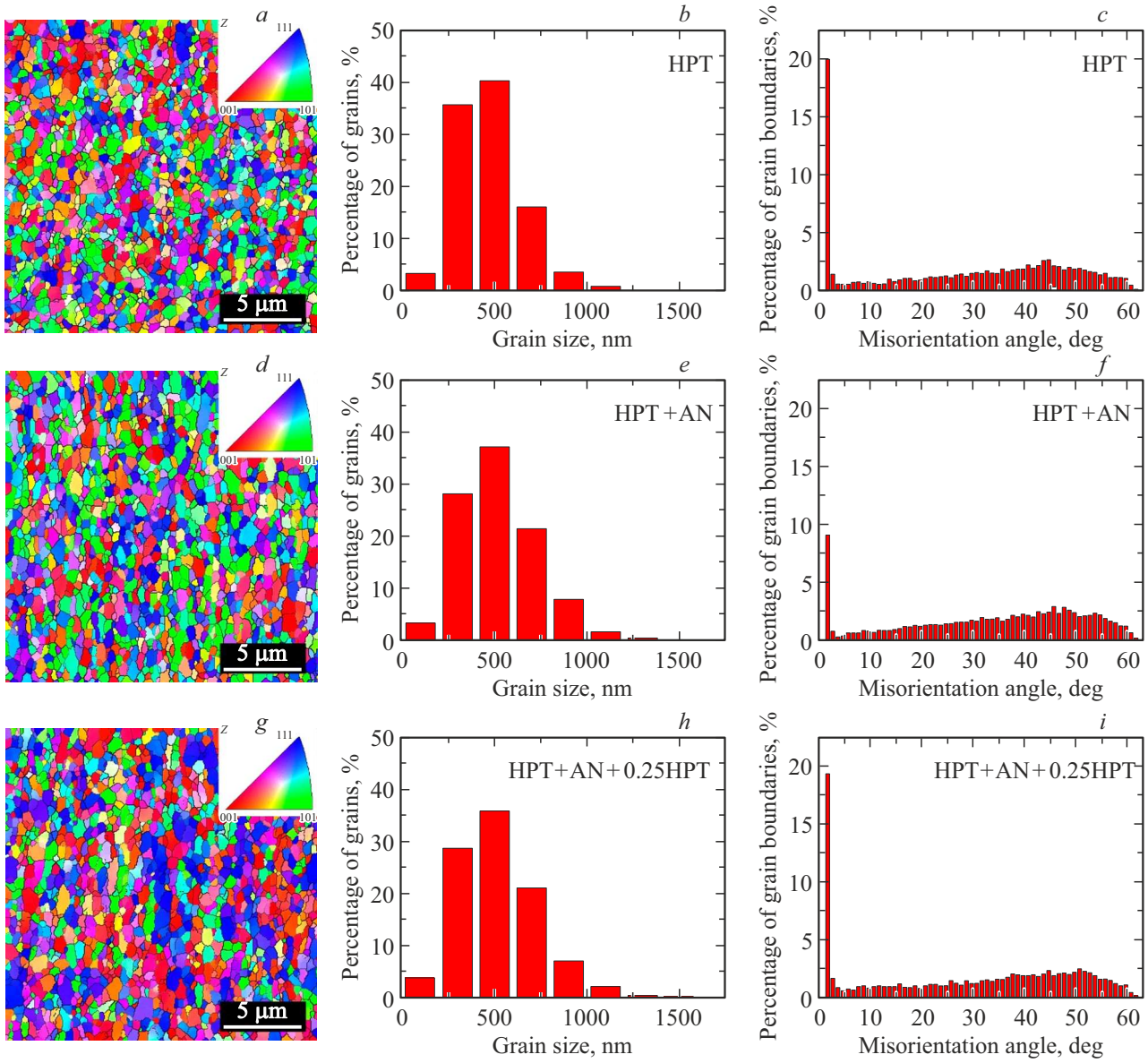

Figure 4. Typical EBSD maps (*a, d, g*) with corresponding grain size distributions (*b, e, h*) and grain boundary distributions on misorientation angles (*c, f, i*) for UFG Al-0.95Mg-0.32Zr (wt.%) alloy in various states: HPT (*a, b, c*), HPT+AN (*d, e, f*), and HPT+AN+0.25HPT (*g, h, i*).

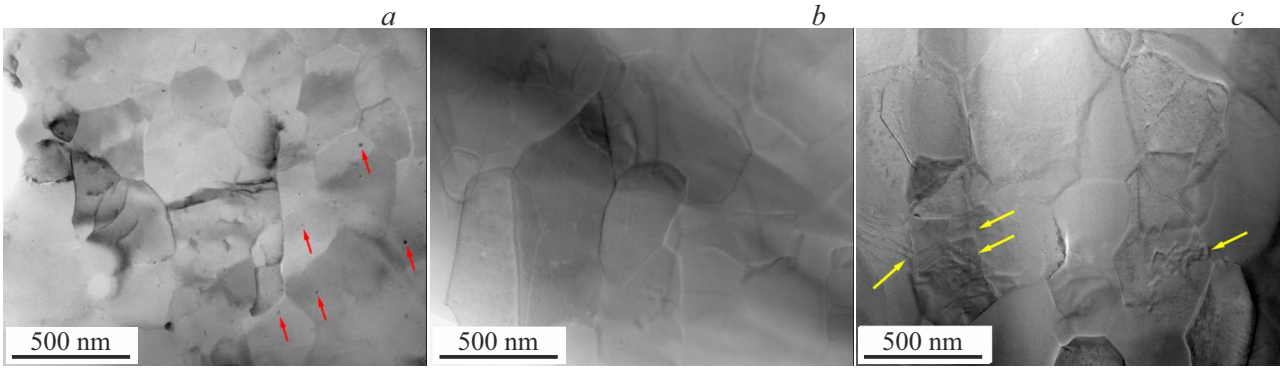

Figure 5. Typical TEM images of UFG Al-0.95Mg-0.32Zr (wt.%) alloy in various states: HPT (*a*), HPT+AN (*b*), and HPT+AN+0.25HPT (*c*). Nanoprecipitates of Al_3Zr phase are shown by red arrow in (*a*). Dislocations entering/exiting grain boundaries are shown by yellow arrows in (*c*).

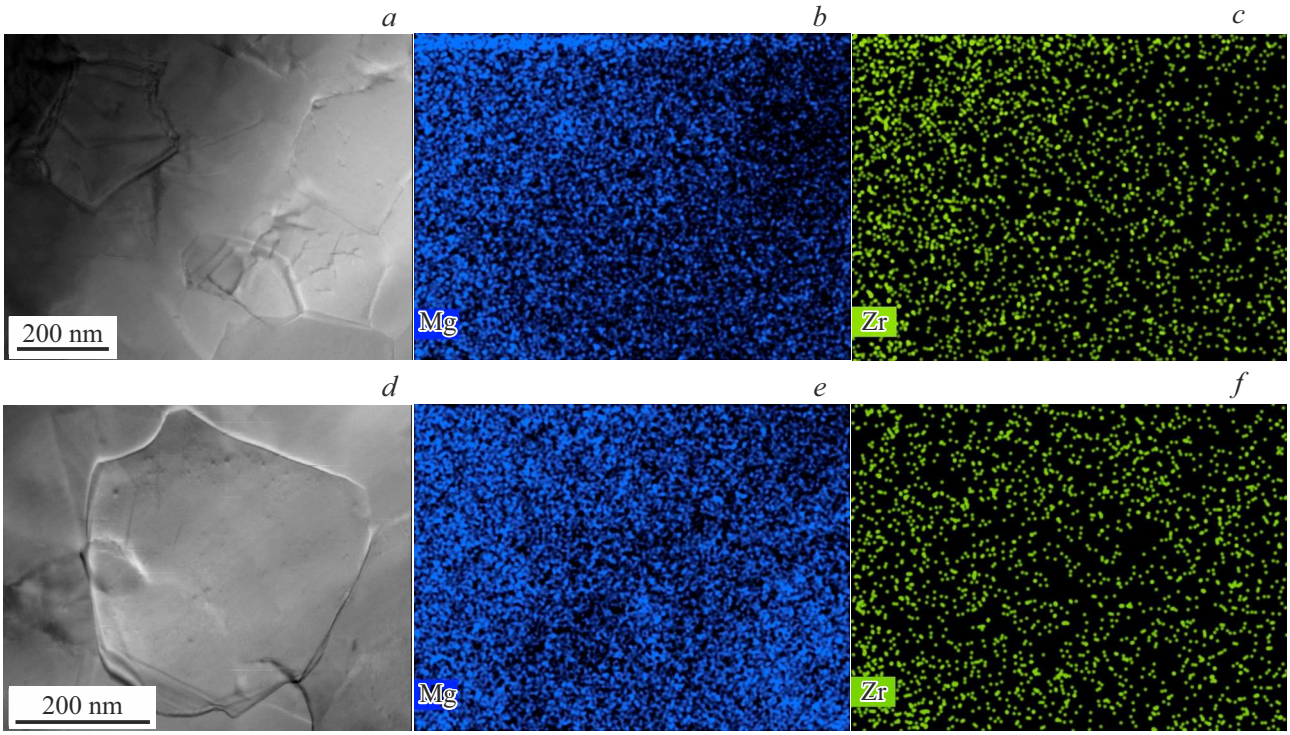

Figure 6. STEM image with corresponding distributions of selected alloying elements (Mg, Zr) for the UFG Al-0.95Mg-0.32Zr (wt.%) alloy in HPT (*a, b, c*) and HPT+AN+0.25HPT (*d, e, f*) states, STEM-EDX analysis.

elements dissolved in the aluminum matrix, the obtained result also indirectly indicates that the concentration of the alloying elements Zr and Mg in the solid solution does not change after DHT. Earlier we showed for UFG Al-0.53Mg-0.27Zr (wt.%) alloy by atom probe tomography (APT) that Mg atoms are located mainly in aluminum matrix in solid solution [28]. No Mg-contained secondary phases were found by the EDX mapping *in-situ* in STEM also at present work. The examples of the EDX maps for the HPT and HPT+AN+0.25HPT states of UFG Al-0.95Mg-0.32Zr (wt.%) alloy are shown in Figure 6.

No intermetallic phases were also revealed by XRD and Mg element mapping in STEM [37] and APT [38] experiments for HPT-processed Al-Mg alloys with Mg content up to 8 wt.%. As was noted in [37], HPT significantly elevates the solid solubility of Mg atoms, thereby impeding the precipitation of intermetallic compounds. In addition to the Mg location in the solid solution in grains, Mg segregates at GBs during the formation of the UFG structure by HPT processing of Al-Mg alloys [37,39].

Segregation of Mg at GBs was also detected in the HPT-processed Al-0.95Mg-0.32Zr (wt.%) alloy (Figure 7). Figure 7 shows a typical HAADF-STEM image (high-angle annular dark-field image in scanning transmission electron microscopy) and concentration profiles of the chemical elements Al, Mg, and Zr in accordance with the results of the EDX analysis performed *in-situ* in STEM for the Al-0.95Mg-0.32Zr (wt.%) alloy in the HPT state. It should be noted that Mg segregation was not clearly recorded in all scans across different GBs, indicating that the segregation of Mg is not uniform among different GBs or/and along GBs. These observations are in agreement with the data reported for HPT-processed Al-Mg alloys [38,39]. Inhomogeneous segregation of Mg and even formation of Mg depletion zones near GBs were observed in HPT-processed Al-Mg alloys [38,39].

XRD analysis (Table 2) showed that the value of the cubic unit cell parameter a of the Al-0.95Mg-0.32Zr (wt.%) alloy remains practically unchanged in all studied states. This indicates that the concentration of Mg in the solid solution remains unchanged after the application of DHT, since it is known that magnesium dissolved in aluminum significantly affects parameter a [40].

The value of dislocation density L_{dis} was determined using average size of the coherently scattering domains D_{CSD} and the average absolute value of microstrain ε_s (or $\langle\varepsilon^2\rangle^{1/2}$) (Table 2), similar to Ref. [18]. After annealing, the value of L_{dis} decreases by ~ 5 times due to recovery processes. Additional HPT deformation to 0.25 turns (HPT+AN+0.25HPT state) leads to the introduction of additional dislocations, returning the value of L_{dis} to that in the HPT state. Since TEM studies do not reveal a large number of dislocations in the grain interiors, it is most likely that the dislocation density determined by analysis of XRD reflection profiles refers mainly to the GBs and near-boundary regions. Thus, the main structural change that occurs in the UFG alloy after annealing and additional

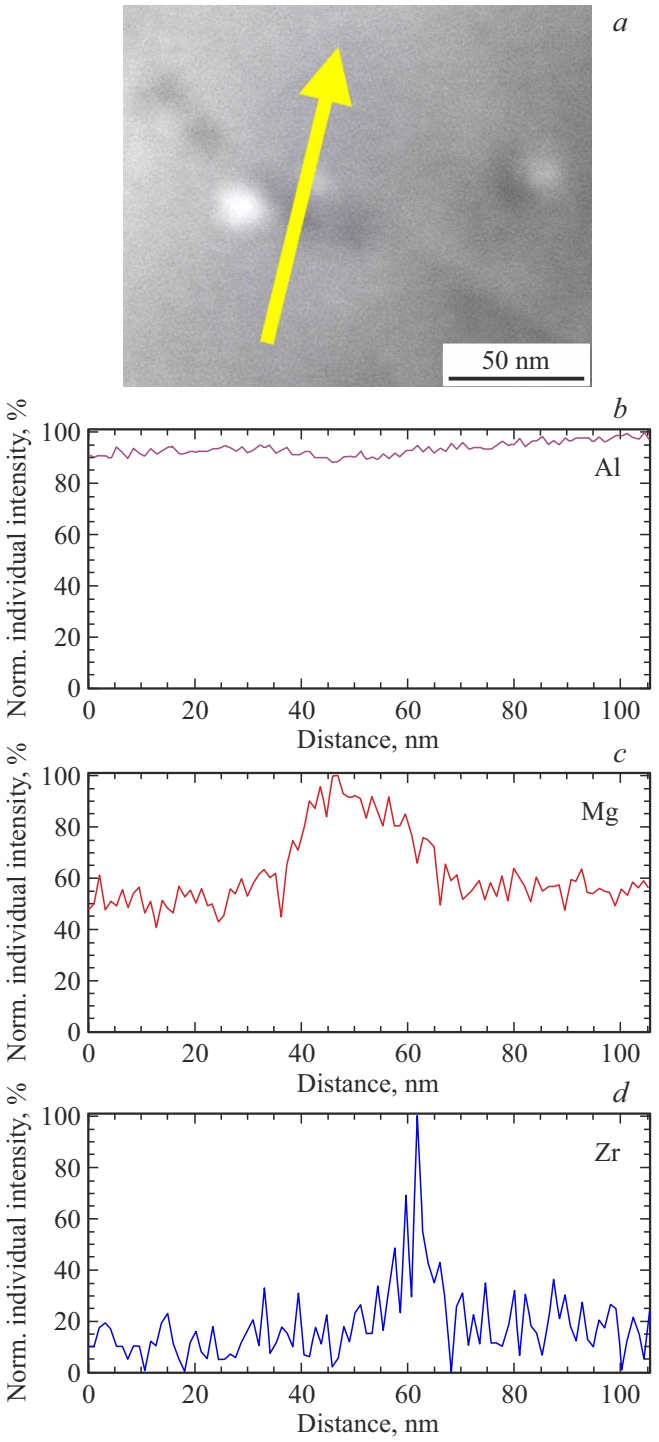

Figure 7. Al-0.95Mg-0.32Zr (wt.%) alloy in HPT state: HAADF-STEM image (*a*) and concentration profiles of Al (*b*), Mg (*c*), and Zr (*d*), each of which is normalized to its maximum, across the grain boundary along the arrow shown in (*a*).

HPT deformation is the change in dislocation density in the GBs and near-boundary regions.

We performed analysis of the fracture surfaces of the fractured samples in the HPT and HPT+AN+0.25HPT states after the tensile tests at different temperatures. Figure 8 shows typical SEM images of the fracture surfaces of samples of UFG Al-0.95Mg-0.32Zr (wt.%) alloy in HPT and HPT+AN+0.25HPT states after their tensile testing at various T_{def}.

The fracture surface of the HPT sample tested at 293 K is rather uniformly covered with small shallow dimples, rare coarser and deeper dimples are also present (Figure 8, *a–b*, highlighted with dotted yellow rectangular). In addition, numerous large brittle facets and a significant number of cracks are clearly observed (Figure 8, *b*, highlighted with dotted white or black rectangles and ellipses, correspondingly), which indicates the brittle fracture [41–43]. With decreasing T_{def}, a decrease in the number of coarse dimples is observed, and at the same time, the density of areas with brittle facets (Figure 8, *c,f*, highlighted by dotted white or black rectangles) as well as the number of cracks increases (Figure 8, *c,f*, highlighted by dotted white or black ellipses). All this clearly indicates the high tendency of HPT samples to brittle fracture at all temperatures studied.

On the fracture surface of the HPT+AN+0.25HPT samples after tensile tests at room temperature (Figure 8, *g–h*), a dimpled relief which is characteristic of ductile fracture [41–44] is observed. This relief contains a large number of equiaxed fine dimples and a much smaller number of coarse deep dimples (highlighted with yellow dotted rectangles in Figure 8, *h*). A small number of brittle facets is also present (highlighted with white dotted rectangles in Figure 8, *h*). Thus, the mode of fracture is mixed, similarly to the HPT state, but with much more pronounced features of ductile fracture. In contrast to the HPT state, in the HPT+AN+0.25HPT state, an increase in the number, as well as in the size and depth of dimples is observed with decreasing tensile test temperature (Figure 8, *i–l*). Moreover, the density and size of brittle fracture features are significantly less than in the HPT state. All this indicates a more ductile nature of the fracture of the HPT+AN+0.25HPT samples compared to the HPT samples in the temperature range 77–293 K, that well correlates with the values of ductility measured in the tensile tests (Table 1).

4. Discussion

The increase in strength with a decrease in temperature observed for HPT and HPT+AN states (Figure 2, *a*) is typical for both CG and UFG Al-based alloys [2,19,26]. In the HPT+AN+0.25HPT state, the anomalous decrease in $\sigma_{0.2}$ and increase in ductility with a decrease in the deformation temperature from 293 to 243 K (Figure 2) can be explained within the framework of the model proposed for explanation of DIS effect at RT in [15]. According to this model, an additional deformation of 0.25HPT leads to the introduction of EGBDs forming dislocation pile-ups in GBs at triple junctions (TJs) under loading [15]. Such pile-ups promote emission of lattice dislocations from the GBs, leading to an increase in ductility with a slight

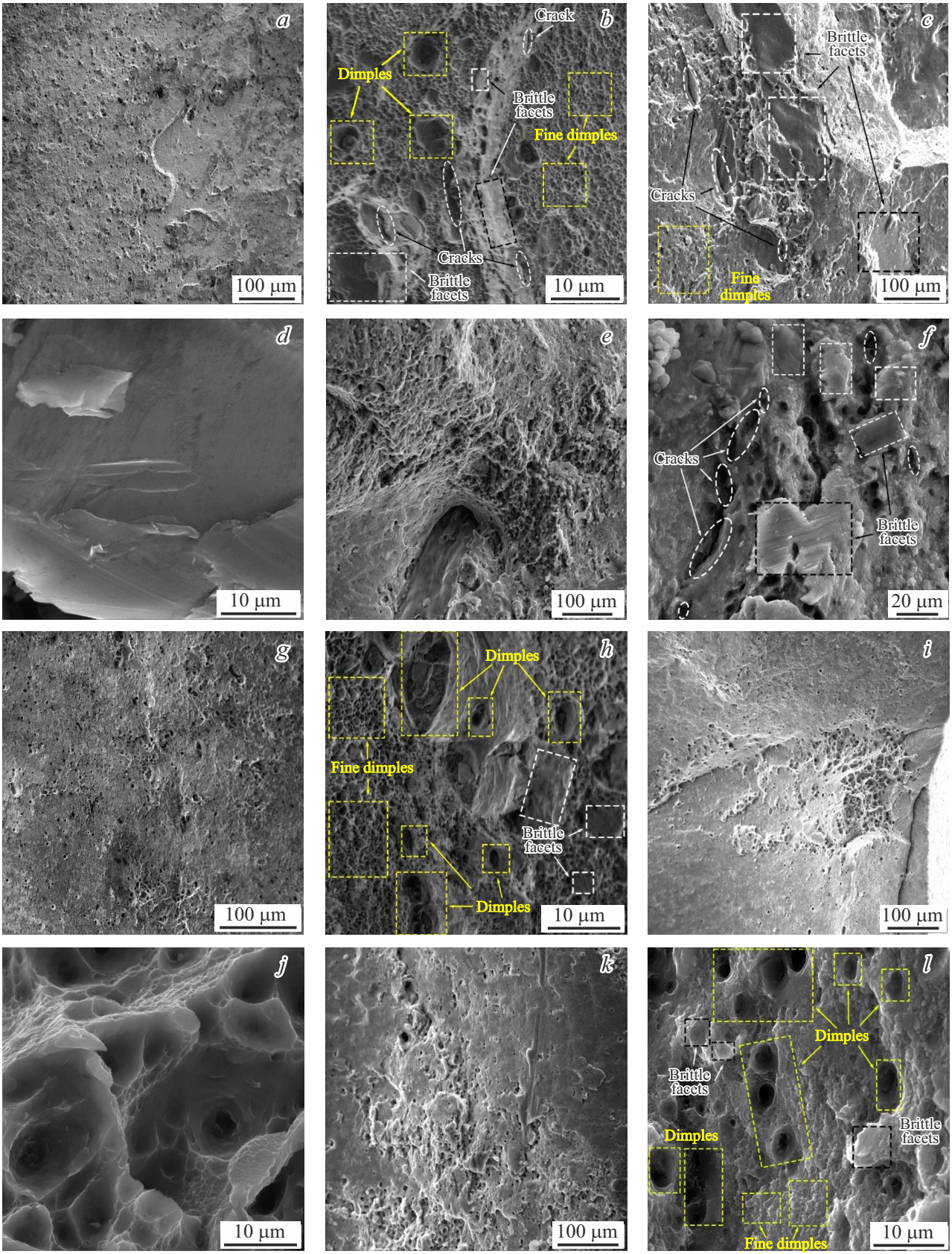

Figure 8. SEM micrographs of fracture morphologies for samples of the UFG Al-0.95Mg-0.32Zr (wt.%) alloy in HPT (*a–f*) and HPT+AN+0.25HPT (*g–l*) states, tested at various deformation temperatures: 293 K (*a, b* and *g, h*); 243 K (*c, d* and *i, j*); 77 K (*e, f* and *k, l*).

decrease in strength. Due to the small magnitude and short duration of additional 0.25 HPT deformation, the introduced EGBDs are not pined by Mg atoms, and therefore they can move along GB plane and form pile-ups at TJs under external shear stress. Then the anomalous change in $\sigma_{0.2}$ and δ in the temperature range 243–293 K is determined by thermally activated processes affecting the mobility of the EGBDs, and, hence, the formation of pile-ups at TJs. Such processes can be dynamic strain aging (DSA) [45–47] and overcoming the Peierls barrier in GBs by grain boundary dislocations moving along the grain boundaries [24], which have an opposite effect on the mobility of EGBDs with decreasing T_{def}. As T_{def} decreases, the diffusivity of solute atoms decreases, which results in an increase in the time required for the pinning of moving EGBDs by Mg atoms [48]. This will enhance the mobility of EGBDs. On the contrary, the time for overcoming the GBs Peierls barrier by moving EGBDs increases with decrease in T_{def}, decreasing their mobility. Apparently, in the temperature range of 243–293 K, the DSA process dominates. As a result, powerful pile-ups are formed at the GBs, and the ductility increases, but the strength decreases.

With a further decrease in T_{def}, the characters of the $\sigma_{0.2}(T_{def})$ and $\delta(T_{def})$ dependences are similar in all states studied (Figure 2). Probably, in the deformation temperature range of 77–243 K, there is no sufficient time for the formation of EGBDs pile-ups during loading, and another mechanism of plastic deformation determines the character of the temperature dependences of $\sigma_{0.2}$. The movement of emitted lattice dislocations across the grains could be such process. Since the diffusivity of solute atoms in the bulk is much lower than in GBs and decreases with decreasing deformation temperature, DSA processes may not operate in the bulk. This can explain the normal character of the $\sigma_{0.2}(T_{def})$ dependences in the temperature range of 77–243 K for the Al-0.95Mg-0.32Zr (wt.%) alloy in both states (HPT and HPT+AN+0.25HPT).

The plastic deformation of metals and alloys can be described by the conventional power law [49,50]:

$$\dot{\varepsilon} = A\sigma^n \exp\left(\frac{Q}{RT}\right), \qquad (2)$$

where A is a material constant, $n = 1/m$ is the stress exponent, m is the strain rate sensitivity, Q is the activation energy, R is the gas constant, T is the absolute temperature, and $\dot{\varepsilon}$ is the strain rate. The Q value can be determined from the slope of a straight line fit to the $(\ln\sigma - 1/T)$ data at a constant strain rate $\dot{\varepsilon}$.

In Ref. [51], the activation energy of plastic flow in an HPT-processed (4N) Al was estimated from the dependence of $\sigma_{0.2}(T)$, where $\sigma_{0.2}$ was determined as $\sigma_{0.2} = 1/3H_V$ (H_V is microhardness) in depth-sensing micro- and nanoindentation experiments ($m \approx 0.03$ and $Q \approx 87$ kJ/mol [51]). Then, supposing that the values of $\sigma_{0.2}$ do not differ much in tensile tests and depth-sensing micro- and nanoindentation experiments, the Q value was estimated for the HPT-processed CP Al from the $\sigma_{0.2}(T)$ dependence obtained in tensile tests [25]. The obtained Q value in the tensile tests [25] was in good agreement with that in [51].

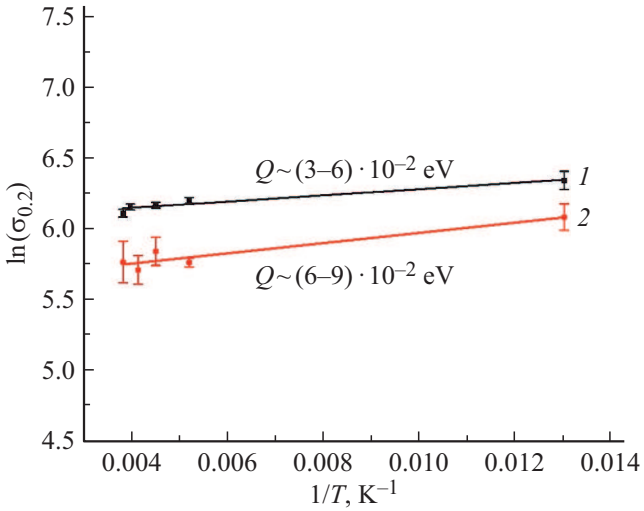

Figure 9. Evaluation of the activation energy (Q) for the Al-0.95Mg-0.32Zr (wt.%) alloy in different states: HPT (curve *1*), HPT+AN+0.25HPT (curve *2*).

In a similar way, we estimated the activation energy Q of the beginning of plastic flow in the range of 77–243 K for the Al-0.95Mg-0.32Zr (wt.%) alloy before and after DHT (in the HPT and HPT+AN+0.25HPT states).

The Q value was determined from the slope of a straight line fit to the $(\ln\sigma_{0.2} - 1/T_{def})$ data at a constant strain rate of $5 \cdot 10^{-4}$ s^{-1} (Figure 9). Taking into account that the m value is 0.055 and 0.033, respectively, in Al-0.53Mg-0.32Zr (wt.%) [18] and Al-1.17Mg-0.33Zr (wt.%) alloys in both states (HPT and HPT+AN+0.25HPT), the value of m was assumed to be 0.033–0.055. The obtained values of Q, equal to 0.04–0.09 eV, are comparable with the activation energies of kink formation for lattice dislocations ($E \sim 0.09$ eV in pure Al [52,53]). This supports our assumption that the temperature behavior of the flow stress in the temperature range of 77–243 K is determined by the movement of the emitted lattice dislocations inside the grains.

Then, a significantly higher ductility in the HPT+AN+0.25HPT state compared with that in the HPT state is most probably associated with the presence of substantial number of unpinned EGBDs in GBs in the first case, the emission of which is easier than of the pinned dislocations and can provide enhanced ductility. However, additional research is required to confirm or refute this hypothesis and to develop a theoretical model that can describe the obtained anomalous temperature behavior of $\sigma_{0.2}$ and δ at decreased deformation temperatures. This is a challenge for further research.

According to Ref. [54,55], the absorption of dislocations at grain boundaries can play a significant role in the plastic deformation of UFG and NC alloys. Nonequilibrium GBs possess a higher absorption efficiency compared to

equilibrium GBs and, as a consequence, can promote better ductility. Then, with a decrease in T_{def}, the ductility should decrease due to the lower ability of the GBs to absorb dislocations, since the coefficient of grain boundary diffusion decreases. However, mechanical tests of the HPT+AN+0.25HPT state show the opposite result. Thus, the absorption processes at GBs do not play the key role in the anomalous temperature dependence of ductility in the case under study.

5. Conclusions

The effect of deformation temperature on strength and ductility of HPT-processed Al-0.95Mg-0.32Zr (wt.%) alloy before and after a special deformation-heat treatment has been studied for the first time. It has been shown that DHT consisting of low-temperature annealing and subsequent additional small deformation leads to substantial increase of ductility while maintaining high strength. The achieved enhanced ductility ($\delta \sim 7-13\%$) with high strength ($\sigma_{0.2} \sim 300-435$ MPa, $\sigma_{UTS} \sim 370-490$ MPa) is kept in the entire temperature range 77–293 K of tensile tests that is highly important for potential application at low temperatures. An anomalous character of the temperature dependences of $\sigma_{0.2}$ and δ in the deformation temperature range of 243–293 K was revealed for the first time for the UFG Al-0.95Mg-0.32Zr (wt.%) alloy after DHT. Transformation of dislocation structure of grain boundaries, which is caused by DHT, is the key factor responsible for such anomalous change of mechanical properties with temperature. A possible explanation for this anomalous behavior is proposed.

The results obtained showed the fundamental possibility of remarkable modulation of the mechanical properties of UFG Al-Mg-Zr alloys in a wide range of low temperatures (77–293 K) due to changes of GB state in the UFG structure without changing the grain size.

Acknowledgements

The XRD, EBSD, TEM and STEM investigations were carried out using the equipment and software of the Center of Joint Use „Materials Science and Diagnostics in Advanced Technologies“ (Ioffe Institute, St. Petersburg, Russia). The authors are grateful to D.A. Kalganov for conducting factography research using scanning electron microscopy.

Funding

This work was financially supported by the Russian Science Foundation [grant number 22-19-00292].

Conflict of interest

The authors declare that they have no conflict of interest.

References

[1] K. Son, M.E. Kassner, T.K. Lee, J.W. Lee. Mater. Des. **224**, 111336 (2022). https://doi.org/10.1016/j.matdes.2022.111336
[2] D.H. Park, S.W. Choi, J.H. Kim, J.M. Lee. Cryogenics **68**, 44 (2015). https://doi.org/10.1016/j.cryogenics.2015.02.001
[3] W.S. Park, M.S. Chun, M.S. Han, M.H. Kim, J.M. Lee. Mater. Sci. Eng. A **528**, *18*, 5790 (2011). https://doi.org/10.1016/j.msea.2011.04.032
[4] K. Edalati, A. Bachmaier, V.A. Beloshenko, Y. Beygelzimer, V.D. Blank, W. Botta et all. Mater. Res. Lett. **10**, *4*, 163 (2022). https://doi.org/10.1080/21663831.2022.2029779
[5] D.C. Machado, P.C.A. Flausino, Y. Huang, P.R. Cetlin, T.G. Langdon, P.H.R. Pereira, J. Mater. Res. Technol. **24**, 2850 (2023). https://doi.org/10.1016/j.jmrt.2023.03.167
[6] E. Damavandi, S. Nourouzi, S.M. Rabiee, R. Jamaati, J.A. Szpunar. J. Mater. Sci. **56**, 3535 (2021). https://doi.org/10.1007/s10853-020-05479-5
[7] X.M. Mei, Q.S. Mei, J.Y. Li, C.L. Li, L. Wan, F. Chen, Z.H. Chen, T. Xu, Y.C. Wang, Y.Y. Tan. J. Mater. Sci. Technol. **125**, 238 (2022). https://doi.org/10.1016/j.jmst.2022.02.029
[8] K. Changela, H. Krishnaswamy, R.K. Digavalli, Mater. Sci. Eng. A **760**, 7 (2019). https://doi.org/10.1016/j.msea.2019.05.088
[9] Z. Be'zi, G. Kra'llics, M. El-Tahawy, P. Pekker, J. Gubicza. Mater. Sci. Eng. A **688**, 210 (2017). https://doi.org/10.1016/j.msea.2017.01.112
[10] A.S. Al-Zubaydi, N. Gao, S. Wang, P.A. Reed. J. Mater. Sci. **57**, *19*, 8956 (2022). https://doi.org/10.1007/s10853-022-07234-4
[11] M. Howeyze, A.R. Eivani, H. Arabi, H.R. Jafarian. Mater. Sci. Eng. A **732**, 120 (2018). https://doi.org/10.1016/j.msea.2018.06.081
[12] X. Li, W. Xia, J. Chen, H. Yan, Z. Li, B. Su, M. Song. Met. Mater. Int. **27**, 1 (2021). https://doi.org/10.1007/s12540-020-00929-w
[13] Y.H. Zhao, X.Z. Liao, S. Cheng, E. Ma, Y.T. Zhu. Adv. Mater. **18**, 17, 2280 (2006). https://doi.org/10.1002/adma.200600310
[14] A.M. Mavlyutov, T.A. Latynina, M.Y. Murashkin, R.Z. Valiev, T.S. Orlova. Phys. Solid State **59**, 1970 (2017). https://doi.org/10.1134/S1063783417100274
[15] T.S. Orlova, N.V. Skiba, A.M. Mavlyutov, M.Y. Murashkin, R.Z. Valiev, M.Y. Gutkin. Rev. Adv. Mater. Sci. **57**, *2*, 224 (2018). https://doi.org/10.1515/rams-2018-0068
[16] X. Huang, N. Hansen, N. Tsuji. Science **312**, *5771*, 249 (2006). https://doi.org/10.1126/science.1124268
[17] T.S. Orlova, D.I. Sadykov, D.A. Kirilenko, A.I. Lihachev, A.A. Levin. Mater. Sci. Eng. A **875**, 145122 (2023). https://doi.org/10.1016/j.msea.2023.145122
[18] T.S. Orlova, A.M. Mavlyutov, D.I. Sadykov, N.A. Enikeev, M.Y. Murashkin. Metals **13**, *9*, 1570 (2023). https://doi.org/10.3390/met13091570
[19] D. Zhemchuzhnikova, R. Kaibyshev. Adv. Eng. Mater. **17**, *12*, 1804 (2015). https://doi.org/10.1002/adem.201500138
[20] D. Zhemchuzhnikova, S. Malopheyev, S. Mironov, R. Kaibyshev. Mater. Sci. Eng. A **598**, 387 (2014). https://doi.org/10.1016/j.msea.2014.01.060
[21] Y. Ma, C. Liu, K. Miao, H. Wu, R. Li, X. Li, G. Fan. J. Alloys Compd. 947, 169559 (2023). https://doi.org/10.1016/j.jallcom.2023.169559

[22] D.C.C. Magalhães, A.M. Kliauga, V.L. Sordi. Trans. Nonferrous Met. Soc. China **31**, *3*, 595 (2021). https://doi.org/10.1016/S1003-6326(21)65522-X
[23] D.C.C. Magalhães, A.M. Kliauga, M.F. Hupalo, O.M. Cintho, C.A. Della Rovere, M. Ferrante, V.L. Sordi. Mater. Sci. Eng. A **768**, 138485 (2019). https://doi.org/10.1016/j.msea.2019.138485
[24] T.S. Orlova, A.M. Mavlyutov, M.Y. Gutkin. Mater. Sci. Eng. A **802**, 140588 (2021). https://doi.org/10.1016/j.msea.2020.140588
[25] T.S. Orlova, A.M. Mavlyutov, M.Y. Murashkin, N.A. Enikeev, A.D. Evstifeev, D.I. Sadykov, M.Y. Gutkin. Materials **15**, *23*, 8429 (2022). https://doi.org/10.3390/ma15238429
[26] T.S. Orlova, D.I. Sadykov, D.V. Danilov, M.Y. Murashkin. J. Alloys Compd. **931**, 167540 (2023). https://doi.org/10.1016/j.jallcom.2022.167540
[27] P.L. Sun, C.Y. Yu, P.W. Kao, C.P. Chang. Scr. Mater. **52**, *4*, 265 (2005). https://doi.org/10.1016/j.scriptamat.2004.10.022
[28] T.S. Orlova, T.A. Latynina, M.Y. Murashkin, F. Chabanais, L. Rigutti, W. Lefebvre. J. Alloys Compd. **859**, 157775 (2021). https://doi.org/10.1016/j.jallcom.2020.157775
[29] P.H.L. Souza, C.A.S. de Oliveira, J.M. do Vale Quaresma. J. Mater. Res. Technol. **7**, *1*, 66 (2018). https://doi.org/10.1016/j.jmrt.2017.05.006
[30] G.K. Williamson, R.E. Smallman III. Philos. Mag. **1**, *1*, 34 (1956). https://doi.org/10.1080/14786435608238074
[31] J. Hirth, I. Lothe. Theory of Dislocations. Atomizdat, Moscow. (1972). 600 p.
[32] T.S. Orlova, T.A. Latynina, A.M. Mavlyutov, M.Y. Murashkin, R.Z. Valiev. J. Alloys. Compd. **784**, 41 (2019). https://doi.org/10.1016/j.jallcom.2018.12.324
[33] T.A. Latynina, A.M. Mavlyutov, M.Y. Murashkin, R.Z. Valiev, T.S. Orlova. Phil. Mag. **99**, *19*, 2424 (2019). https://doi.org/10.1080/14786435.2019.1631501
[34] K.E. Knipling, D.C. Dunand, D.N. Int. J. Mater. Res. **97**, *3*, 246 (2022). https://doi.org/10.1515/ijmr-2006-0042
[35] A.V. Mikhaylovskaya, A.G. Mochugovskiy, V.S. Levchenko, N.Yu. Tabachkova, W. Mufalo, V.K. Portnoy. Mater. Charact. **139**, 30 (2018). https://doi.org/10.1016/j.matchar.2018.02.030
[36] M. Zha, H. Zhang, H. Jia, Y. Gao, S. Jin, G. Sha, R. Bjørge, R.H. Mathiesen, H.J. Roven, H. Wang, Y. Li. Int. J. Plast. **146**, 103108 (2021). https://doi.org/10.1016/j.ijplas.2021.103108
[37] C. Chen, Y. Chen, J. Yu, M. Liu, J. Zhang. J. Alloys. Compd. **983**, 173905 (2024). https://doi.org/10.1016/j.jallcom.2024.173905
[38] J. Xue, S. Jin, X. An, X. Liao, J. Li, G. Sha. J. Mater. Sci. Technol. **35**, *5*, 858 (2019). https://doi.org/10.1016/j.jmst.2018.11.017
[39] Y. Liu, M. Liu, X. Chen, Y. Cao, H.J. Roven, M. Murashkin, R.Z. Valiev, H. Zhou. Scr. Mater. **159**, 137 (2019). https://doi.org/10.1016/j.scriptamat.2018.09.033
[40] J.E. Hatch. Aluminum: properties and physical metallurgy. 1st ed. ASM International: Metals Park, OH (1984). 424 p.
[41] J.L. González-Velázquez. Fractography and failure analysis. Springer International Publishing, Switzerland (2018). 165 p.
[42] M.K. Pathak, A. Joshi, K.K.S. Mer. Trans. Indian Inst. Met. **74**, 679 (2021). https://doi.org/10.1007/s12666-021-02198-6
[43] ASM Handbook Volume 12: Fractography. 9th ed. ASM International: Metals Park, OH. (1987). 517 p.
[44] G. Wang, D. Song, Z. Zhou, Y. Liu, N. Liang, Y. Wu, A. Ma, J. Jiang. J. Mater. Res. Technol. **15**, 2419 (2021). https://doi.org/10.1016/j.jmrt.2021.09.085
[45] D. Zhou, X. Zhang, H. Wang, Y. Li, B. Sun, D. Zhang. Int. J. Plast. **157**, 103405 (2022). https://doi.org/10.1016/j.ijplas.2022.103405
[46] J. Kang, X. Liu, T. Wang. Scr. Mater.**224**, 115121 (2023). https://doi.org/10.1016/j.scriptamat.2022.115121
[47] H. Sun, W. Zhang, Y. Xu, Q. Li, X. Zhuang, Z. Zhao. Scr. Mater. **222**, 115025 (2023). https://doi.org/10.1016/j.scriptamat.2022.115025
[48] T. Tian, M. Zha, H.L. Jia, Z.M. Hua, P.K. Ma, H.Y. Wang. Mater. Sci. Eng. A **880**, 145376 (2023). https://doi.org/10.1016/j.msea.2023.145376
[49] D. Bae, S.H. Kim, D.H. Kim, W.T. Kim. Acta Mater. **50**, 2343 (2002). https://doi.org/10.1016/S1359-6454(02)00067-8
[50] X.R. Zhang, G.X. Sun, W. Zai, Y. Jiang, Z.H. Jiang, S. Han, G.L. Bi, D.Q. Fang, J.S. Lian. Mater. Sci. Eng. A **799**, 140141 (2021). https://doi.org/10.1016/j.msea.2020.140141
[51] N.Q. Chinh, T. Csanádi, T. Györi, R.Z. Valiev, B.B. Straumal, M. Kawasaki, T.G. Langdon. Mater. Sci. Eng. A **543**, 117 (2012). https://doi.org/10.1016/j.msea.2012.02.056
[52] D. Hull, D.J. Bacon. Introduction to dislocations. 5th ed. Elsevier, Butterworth-Heinemann, Oxford. (2011). 272 p.
[53] V.I. Vladimirov. The physical theory of plasticity and strength. Ch. I. LPI, L. (1973). 120 p. (in Russian)
[54] O. Renk, A. Hohenwarter, V. Maier-Kiener, R. Pippa. J. Alloys Compd. **935**, 168005 (2023). https://doi.org/10.1016/j.jallcom.2022.168005
[55] O. Renk, V. Maier-Kiener, I. Issa, J.H. Li, D. Kiener, R. Pippan. Acta Mater. **165**, 409 (2019). https://doi.org/10.1016/j.actamat.2018.12.002